Oral presentation | Numerical methods

Numerical methods-III

Wed. Jul 17, 2024 10:45 AM - 12:45 PM Room A

[7-A-04] Numerical Simulation of propeller slip-stream influence on the high lift configuration with Actuator Disk Method

*Longyuan YANG[1], Yunyi SHENG[1], Yong YANG[1] (1. Northwestern Polytechnical University)

Keywords: ADM, CFD, Slipstream, High Lift Devises, Steady

Twelfth International Conference on
Computational Fluid Dynamics (ICCFD12),
Kobe, Japan, July 14-19, 2024

Numerical Simulation of propeller slip-stream influence on the high lift configuration with Actuator Disk Method

Longyuan YANG, Yunyi SHENG, Yong YANG*
Corresponding author: yyang@nwpu.edu.cn
*National Key Laboratory of Science and Technology on Aerodynamic Design and Research, Northwestern Polytechnical University, Xian 710072, China

Abstract: With short takeoff and landing distance, high climb rate, low fuel consumption, propeller powered aircraft has its huge remarkable advantage in the short and medium rang transportation field, especially with low demands on the runway. During the takeoff, climb and landing, the propeller slipstream provides considerable extra lift with high lift devises in slipstream zone fully extended. To achieve fast and accurate evaluation of the propeller slipstream effects on high lift devises, this paper employs unsteady Reynolds-averaged Navier-Stoke (URANS) rotating full blades method (FBM) and steady RANS actuator disk method (ADM) embedded in computational fluid dynamics (CFD) simulation. The FBM offers a high fidelity when simulating the influence of propeller slipstream on the high lift configuration. One purpose of this study is to verify the ADM agreement of predicting propeller slipstream by comparing with FBM results under the numerical simulation. The time average loads of ADM can be extracted from an isolated rotating propeller or the full rotating propeller mounted in front of high lift configuration, it is evident that even there are some differences in the load transition, the results of the ADM are basically the same. The simulation results show a good agreement between the pressure distribution of wing and flaps and lift increase due to the propeller slipstream driven by unsteady rotating FBM and ADM approximation. Two different advance ratio cases with fixed propeller rotating speed and different freestream velocity are simulated to show the influence of the thrust strength on the lift increasement, and compared with the power off layout with AOA from -4° to 24°. As the ADM is performed with steady strategy and saves enormous CPU consumption, it can be adopted as an efficient tool for the design of the high lift system with propeller slipstream effect being considered.

Keywords: FBM; ADM; CFD; Propeller slipstream; High lift devices

1. Introduction

Propeller powered aircrafts are featured with short takeoff and landing distance, steep climb, and low fuel consumption [1], these evident advantages make the propeller powered aircraft shares large air transportation market and fits the requirement of military demands. The well-known examples are C-130 and A400M. With the help of the strong propeller slipstream [2, 3, 4], these transportation aircrafts gain a considerable lift increase in takeoff, climb and landing phase. In the takeoff and climb phase, the lifting device greatly improves the lift coefficient of the propeller aircraft. The lift increment of high lift device makes the design is particularly important, considering the influence of propeller slipstream. Accurate prediction of the airflow over a high lift configuration aircraft remains a significant challenge due to the interrelated phenomena of transition, complex surface topology, complex strain fields, and nonequilibrium separated turbulent flow [5].

Nowadays, CFD methods are more and more applied to predict the aerodynamic performance [6, 7], even to simulate the propeller slipstream driven by rotating full blades and its influence acting on the high lift configuration. One thing should be noticed is that, this must be done in unsteady mode with high CPU time.

The unsteady simulation of the rotating full blades gives time accurate propeller slipstream development [8], and reflects detailed action due to the flow pulsation on the high lift system. The time accurate method can provide the details of unsteady interaction. Although the extreme CPU time requirement limits its practical application in the aerodynamic design and performance prediction, FBM uses URANS to predict the propeller slipstream which can accurately simulate the unsteady fluctuation of slipstream. This advantage makes the FBM results become an important reference in analyzes when without experimental data.

Time averaged ADM [9] was adopted as an efficient approximation of the driven source of the propeller slipstream. Vincenzo Cusati [10] used the virtual disk model to simulate propeller slipstream by the blade element method. An equivalent actuator disk model [11] of airplane propeller is presented, which takes into consideration such factors as the pressure jump across the disk, swirl velocity of slipstream, variable-pitch propeller, and rotating speed of rotor, etc. Frédéric Le Chuiton [12] utilized the quasi-steady approximation to modelling rotors with actuator disk. Khier W [13] described numerical simulation of the flow around helicopter fuselage-main rotor-tail rotor configurations using the quasi-steady actuator disk approach and the time-accurate simulation that resolves the relative motion of the main and tail rotors with respect to the fuselage. The influence of propeller slipstream on the load distribution [14], the influence of blade angle and the influence of different relative positions are studied. Different ADM [15] were created and analyzed to fit into CFD package [16, 17]. The actuator disk model is presented which is consistent with the classical model of momentum theory of a zero-thickness surface which imposes a discontinuous pressure jump to the flow [18]. Strash D J [19], Amato M [20] and Christopher Wales [21, 22] employed to predict the propeller slipstream influence exerted on the wings or full-aircraft in cruise condition.

The accuracy of the ADM depends on the agreement between the actuator disk loads distribution and the rotating propeller blades loads distribution. The initial actuator disk load distribution is uniform and gradually developed into parabolic distribution, or engineering estimation formula. In this paper, the disk loads distribution of ADM was transitioned from the loads acting on rotating blades, and the corresponding flow field is approached with CFD.

To achieve an engineering practical evaluation method, the creation of propeller slipstream is approximated by the time averaged jump in pressure and rotational momentum jump across a called actuator disk with zero thickness. The time averaged jump which is time averaged, will be introduced as a special boundary condition in the steady numerical procedure. As the time averaged jump is extracted by an isolated rotating propeller, the current numerical simulation with propeller slipstream avoids the complex detailed propeller grid generation together with the full airplane configuration, and huge time consumed for unsteady progress. This makes the fast design and evaluation of the high lift devise possible. As the high lift devise is operated in low flight speed and high trust condition, propeller slipstream makes a further lift increase. This makes the research and analysis of this topic attracts more interest.

To isolate the performance of ADM in the numerical simulation of propeller slipstream, four steps were conducted for the investigation.

1) With the dynamic patch strategy, the flow field with relative motion between the high lift devise and propeller is successfully simulated with URANS mode. Low advance ratios (large thrust), which are corresponding to take off and climb phase, is of the key interest. The URANS FBM results will be used as reference in this paper.

2) The difference of actuator disk (AD) load distribution extracted from the isolated rotating propeller and full rotating propeller mounted in front of high lift configuration was investigated. Both of the previous loads were used to drive the slipstream in front of the high lift configuration, and the agreement of the pressure distribution, as well as lift and drag coefficients was analyzed.

3) Based on the ready prepared load distribution transitioned from the isolated rotating propeller with corresponding flow conditions, the lift increasement due to the propeller slipstream driven by the ADM were simulated for high lift configuration for the AOA from -4° to 24°.

4) The object for the simulation of two different advance ratios is to reveal the influence of the thrust strength on the agreement between FBM and ADM.

2. Computation scheme

2.1. Governing equation

The three-dimensional time-dependent compressible Navier-Stokes equations can be written as equation (1) [23]:

$$\frac{\partial \boldsymbol{W}}{\partial t}+\frac{\partial(\boldsymbol{F}^{i}+\boldsymbol{F}^{v})}{\partial x}+\frac{\partial(\boldsymbol{G}^{i}+\boldsymbol{G}^{v})}{\partial y}+\frac{\partial(\boldsymbol{H}^{i}+\boldsymbol{H}^{v})}{\partial z}=0 \tag{1}$$

In equation (1), $\boldsymbol{W} = (\rho, \rho u, \rho v, \rho w, e)^T$ is the vector of conservative variables, ρ is the density, u, v and w are the components of velocity, e is total energy per unit volume. $\boldsymbol{F}^i$, $\boldsymbol{G}^i$ and $\boldsymbol{H}^i$ are the inviscid flux terms in three coordinate directions. $\boldsymbol{F}^v$, $\boldsymbol{G}^v$ and $\boldsymbol{H}^v$ are the viscous flux terms, which contain heat flux and viscous forces exerted on the body.

$$
\begin{aligned}
\boldsymbol{F}^{i} &= (\rho u, \rho u^{2}+p, \rho uv, \rho uw, u(\rho e+p))^{T} \\
\boldsymbol{G}^{i} &= (\rho v, \rho vu, \rho v^{2}+p, \rho vw, v(\rho e+p))^{T} \\
\boldsymbol{H}^{i} &= (\rho w, \rho wu, \rho wv, \rho w^{2}+p, w(\rho e+p))^{T}
\end{aligned} \tag{2}
$$

$$
\begin{aligned}
\boldsymbol{F}^{v} &= \frac{1}{\mathrm{Re}}(0, \tau_{xx}, \tau_{xy}, \tau_{xz}, u\tau_{xx}+v\tau_{xy}+w\tau_{xz}+q_{x})^{T} \\
\boldsymbol{G}^{v} &= \frac{1}{\mathrm{Re}}(0, \tau_{xy}, \tau_{yy}, \tau_{yz}, u\tau_{xy}+v\tau_{yy}+w\tau_{yz}+q_{y})^{T} \\
\boldsymbol{H}^{v} &= \frac{1}{\mathrm{Re}}(0, \tau_{xz}, \tau_{yz}, \tau_{zz}, u\tau_{xz}+v\tau_{yz}+w\tau_{zz}+q_{z})^{T}
\end{aligned} \tag{3}
$$

Shown in equation (2), p is pressure. In equation (3), the stress tensor components τ_{ij} and the heat flux vector components q_i can be found in numerous text books [24].

2.2. Geometry Model

An isolated rotating propeller from which the time averaged load is extracted is shown in Fig. 1 (a), and the blade airfoil is shown in Fig. 1 (c). Shown in Fig. 1 (b) and (d), is a half model of high lift configuration mounted with propeller and the airfoil shape of main wing and flaps. This paper focuses on investigating the influence of the high lift configuration on the lift and drag by the propeller slipstream in the takeoff and climb phase, regardless of the pitch moment and trimming, and the geometry has the deflecting flap but without tails.

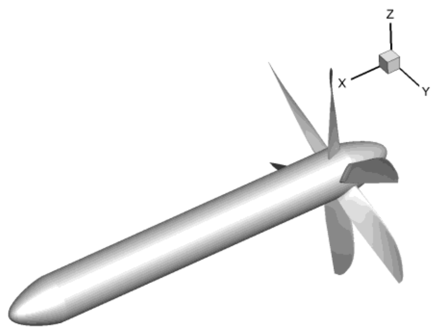

(a) isolated propeller

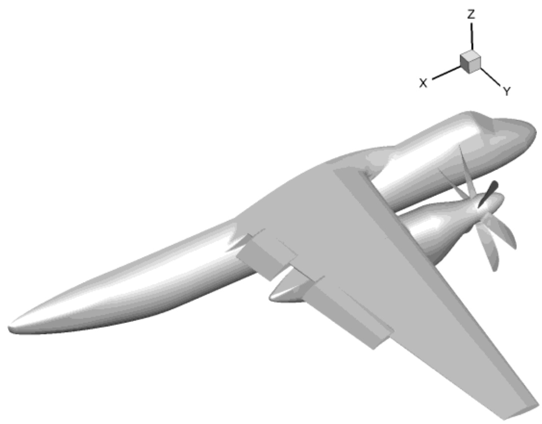

(b) high lift configuration

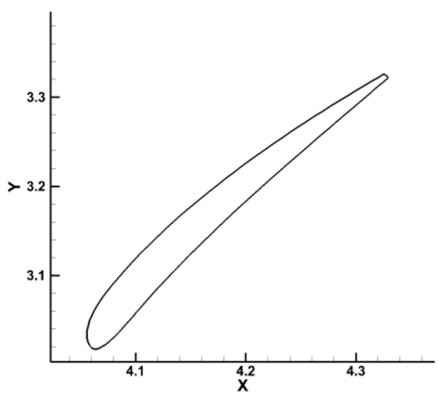

(c) airfoil shape of blade

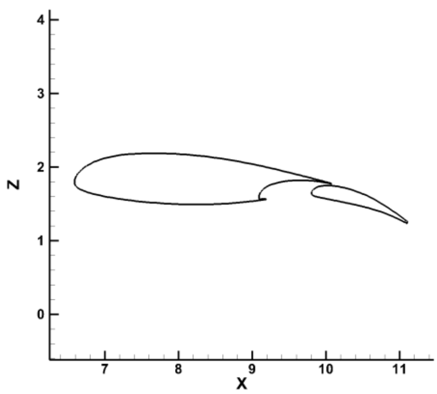

(d) airfoil shape of the wing and flap

Fig. 1 Geometric configuration

The isolated propeller model and high lift configuration geometry have the dimensions given in Table 1.

Table 1 Geometric parameters

r/m	*C/m*	*S/m*^{2}
2.00	3.09	35.00

In Table 1, *r* stands for propeller radius, *C* and *S* represent reference chord and reference surface area of high lift configuration.

2.3. Grid strategy and generation

The FBM involves performing URANS simulations with detailed modelling of the propeller blades. But this approach presents challenges in meshing due to the interaction between a rotating propeller and a static aircraft. The computation structured grid is composed of a background fixed grid and a sub-grid. The sub-grid which contains the real propeller is rotating, the communication between the background and sub-grid is fulfilled with dynamic patching. For ADM simulation, the sub-grid is fixed and without relative motion to the background grid, the communication is carried with point-to-point strategy. Shown in Fig. 2, two types of grid generation techniques are used [25], one is dynamic patched grid for FBM, another is point to point grid for steady actuator disk model. In Fig. 2(a), the structured grid was generated with 46 million points for FBM simulation. Shown in Fig. 2(b), the structured grid was generated with 42 million points for ADM simulation. The grid generation emphasis is on the propeller and disk of high lift configuration. The wing, flap, nacelle and fuselage's topological structure and nodes of the edge are the same except for the propeller slipstream sources.

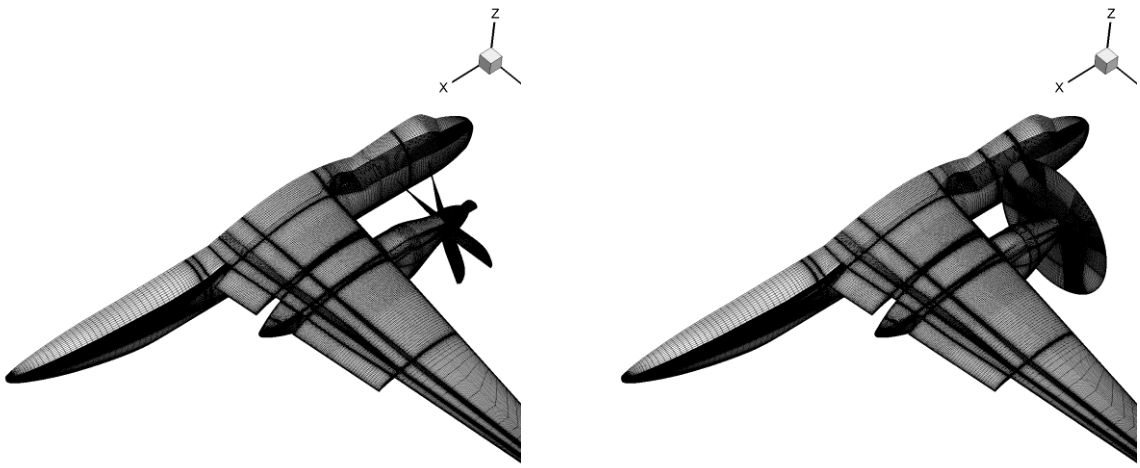

(a) dynamic patched grid for FBM (b) point to point grid for ADM

Fig. 2 Simulation mesh

2.4. Numerical methods for FBM and ADM

The URANS FBM uses dual time-stepping scheme to simulate the propeller slipstream. The rotating propeller has six blades, and one blade passes a fixed point every 60°. To achieve acceptable accuracy in propeller aerodynamics, a time step equivalent to a 1.44° rotation was used to give acceptable accuracy in propeller aerodynamics for situation, resulting in 250-time steps per rotation.

For the ADM, in one rotation period, the driven power of the propeller slipstream can be approximated by a static actuator disk, and the distributed loads on the actuator disk are related to the loads exerted on the real rotating blades by the following equations (4), (5).

$$\Delta p \cdot (rd\theta dr) = \frac{T}{2\pi rdr} \cdot (rd\theta dr) \cdot N \tag{4}$$

$$(\rho u \Delta v_\theta) \cdot (rd\theta dr) = \frac{F_\theta}{2\pi rdr} \cdot (rd\theta dr) \cdot N \tag{5}$$

In equation (4) and (5), Δp is axial pressure jump and $\rho u \Delta v_\theta$ is circumferential momentum jump. One hypothetic actuator element in ADM can be given by time averaged thrust load *T* and circumferential load F_θ, these are the loads acting on *dr* segment of one blade along radial direction. *N* is the number of blades, *r* is the radius of the blade element, *dr* and *rdθ* is the length of the blade element in radius and tangential direction. The FBM blade element and ADM blade element representation is shown in Fig. 3.

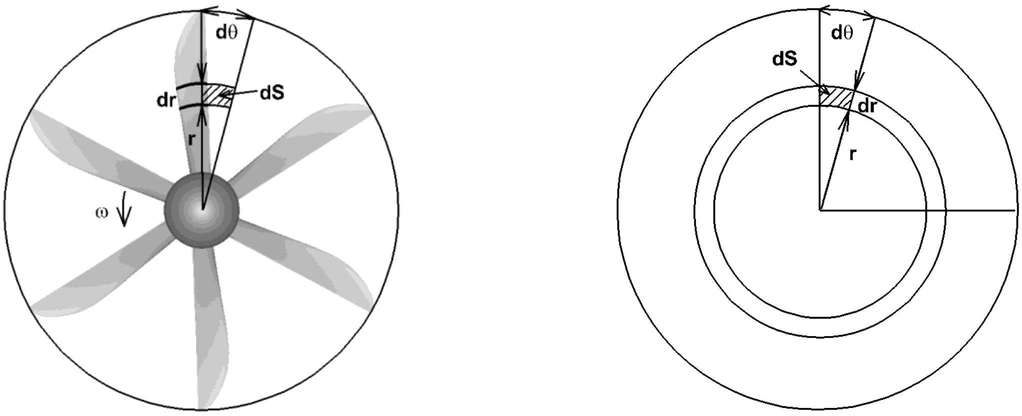

（a） FBM element （b） ADM element

Fig. 3 Loads element

The steady ADM is introduced as a special boundary condition on the interface of two neighboring blocks. The pressure and circumferential momentum jump are added to update flux terms of governing equations across the actuator disk. However, it doesn't change conservative variables directly.

3. Simulation conditions

The present research intents to figure out the influences of propeller slipstream on high lift devices during takeoff and climb phase. The physical flow conditions are given in Table 2.

Table 2 Simulation conditions

	Ma_∞	Re	α/(°)	T_∞/K	n/(round/min)	J	C_T
takeoff	0.1474	3.44×10^6	-4~28	288.15	1075	0.7	0.44
climb	0.2110	4.91×10^6	-4~24	288.15	1075	1.0	0.34

In Table 2, Ma_∞, *Re* stands for free stream Mach number and Renold number; α, T_∞ and J represent angle of attack, free stream temperature and propeller advance ratio, C_T stands for thrust coefficient of propeller at α=0°.

$$J = V_\infty / nD \tag{6}$$

$$C_T = T / \rho n^2 D^4 \tag{7}$$

In equation (6), (7), where V_∞ is the freestream velocity, n the round per seconds, D is the propeller diameter. In this paper, two different advance ratio cases with fixed propeller rotating speed and different freestream velocity are simulated.

4. Results and Analysis

4.1. Vorticity contours

The unsteady FBM was utilized to complete the simulations of the isolated propeller and the full propeller (mounted in front of high lift configuration). The FBM simulation is known for its high accuracy and fidelity, which is closer to the real propeller rotation and aircraft flight situation. Initially the vorticity shed from the isolated propeller and full propeller is preserved well, as shown in Fig. 4.

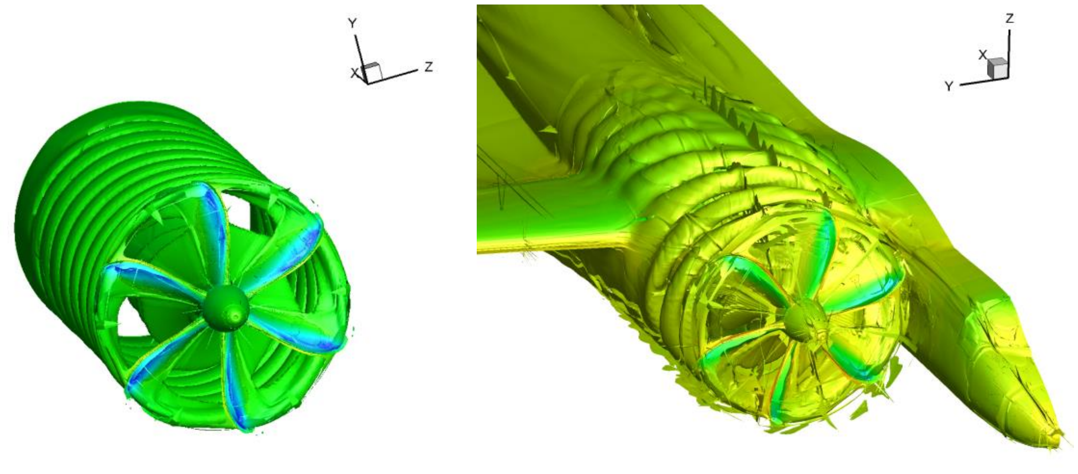

（a） Vorticity of isolated propeller （b） Vorticity of full propeller

Fig. 4 Vorticity contours at J=1.0, α=0°

4.2. Load distribution of Actuator disk

The time averaged loads along the radius at J=0.7, α=16° of the full rotating propeller in front of the high lift configuration and the isolated propeller at four typical sections are shown in Fig. 5. It indicates that the load extracted from full propeller has a slight difference with that from an isolated propeller at section1, section3 and section4, while section2 has further difference than other three sections. It can be noticed from section2 and section4, that both pressure jump and circumferential momentum jump are alternate lead by isolated and full propeller load. But the value of C_T extracted from full propeller is 0.482 and transitioned from isolated propeller is 0.461, the fractional difference is 4.36%.

The comparison of pressure contour with different actuator loads sources is shown in Fig. 6. Four spanwise sections on the wing and flaps are provided, including y/b=0.14, y/b=0.36, y/b=0.44 and y/b=0.52. The comparison of the pressure distribution on main wing and flaps with different actuator loads sources at J=0.7, α=16° is shown in Fig. 7.

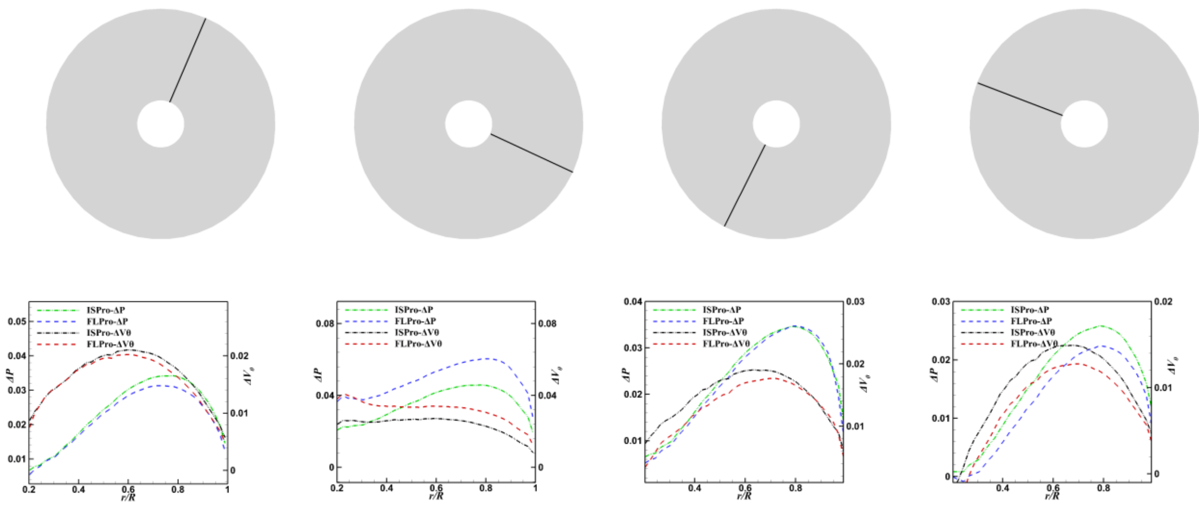

（a） Section1 （b） Section2 （c） Section3 （d） Section4

Fig. 5 Load distribution along radius at the same circumferential station

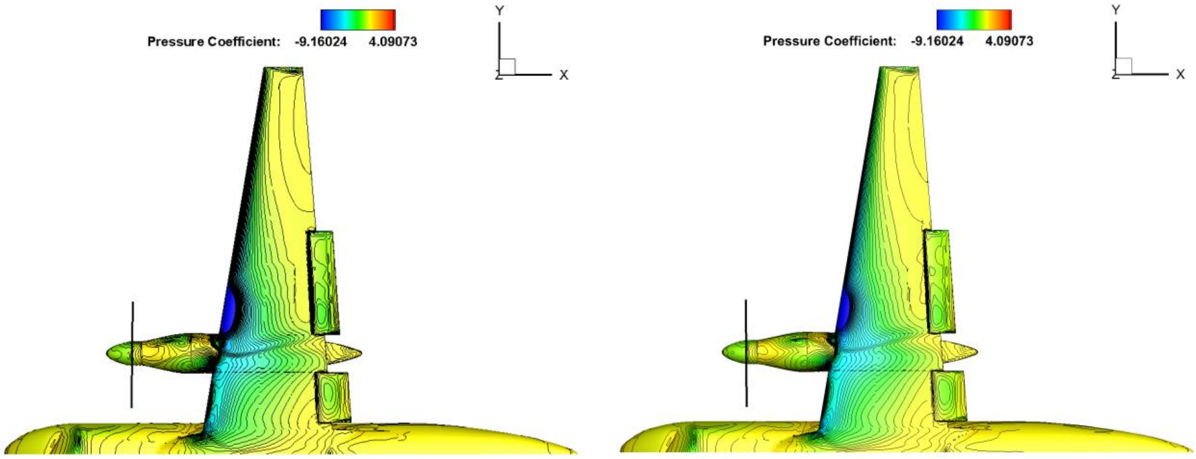

(a) disk loads extracted from full propeller (b) disk loads extracted from isolated propeller

Fig. 6 Comparison of surface pressure with different loads sources at J=0.7, α=16°

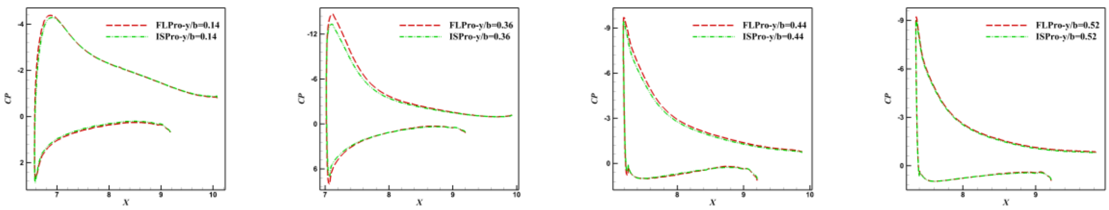

(a) J=0.7, α=16°, wing at y/b=0.14 (b) J=0.7, α=16°, wing at y/b=0.36 (c) J=0.7, α=16°, wing at y/b=0.44 (d) J=0.7, α=16°, wing at y/b=0.52

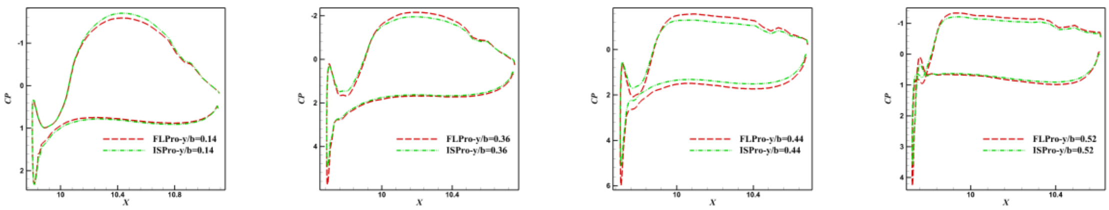

(e) J=0.7, α=16°, flap at y/b=0.14 (f) J=0.7, α=16°, flap at y/b=0.36 (g) J=0.7, α=16°, flap at y/b=0.44 (h) J=0.7, α=16°, flap at y/b=0.52

Fig. 7 Comparison of surface pressure curves with different loads sources at J=0.7, α=16°

In Table 3, where C_L is the lift coefficient, C_D is the drag coefficient and δ is the fractional difference between full propeller result and isolated propeller result.

Table 3 Comparison of lift and drag with different loads sources at J=0.7, α=16°

	Full propeller	Isolated propeller	δ
C_L	3.0687	2.9646	3.39%
C_D	0.6712	0.6464	3.69%

Due to the influences from the wing and fuselage downstream of the propeller, the blade load difference between the isolated and full propeller can be well expected, especially for large attack angles. However, from results in Fig. 6, Fig. 7 and Table 3, it is evident that even there are some differences in the load transitioned from the two different sources, the results of the pressure distribution, as well as lift and drag coefficients are basically the same. It indicates the value of C_T is the dominant factor for the simulation result of the propeller slipstream by ADM.

In Fig. 8, time averaged load distributions of an isolated propeller at J=0.7, α=0° and 16° are displayed on an actuator disk. At α=0°, pressure jump Δp and circumferential swirl velocity jump Δv_θ are axisymmetric. When $\alpha \neq 0°$, the local AOA and velocity change as the blade rotates at different azimuth angle, so does load distribution on the blade.

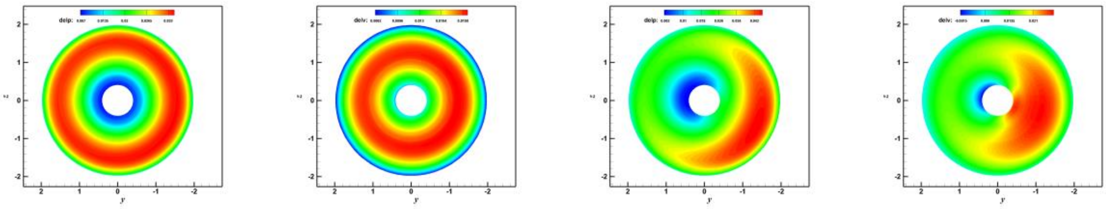

(a) J=0.7, α=0°, Δp (b) J=0.7, α=0°, Δv_θ (c) J=0.7, α=16°, Δp (d) J=0.7, α=16°, Δv_θ

Fig. 8 Load distribution of actuator disk

4.3. Swirling effect

Fig. 9 (a) and (b) represent the effect of loads introduced by rotating blades and actuator disk. Fig. 9 (a) is the space streamline in unsteady FBM propeller slipstream case at α=0°, while Fig. 9 (b) shows space streamline affected by propeller slipstream simulated with ADM. It can be revealed that steady ADM can effectively reflect slipstream swirling caused by rotating propeller.

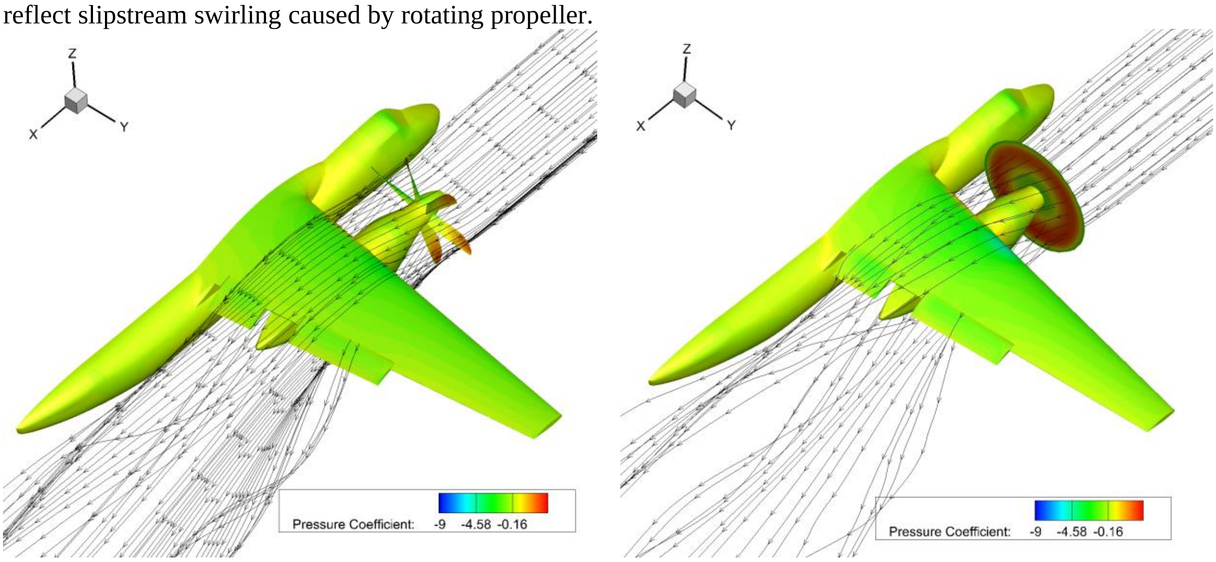

(a) J=0.7, α=0° FBM (b) J=0.7, α=0° ADM

Fig. 9 Local spatial streamline distribution

4.4. Surface pressure contour distribution

Fig. 10 shows surface pressure contour of the high lift configuration with and without slipstream, at α=8° and 16°. The results simulated with unsteady rotating FBM and steady ADM are provided for comparison.

The results given in Fig. 10 (a), (b), (g) and (h) refer to power-off condition. Fig. 10 (c), (e), (i), (k) are unsteady FBM results. The propeller rotates along positive direction of X axis, that means the propeller is in outboard-up mode. Comparing four groups, (a) and (c), (b) and (e), (g) and (i), (h) and (k), on upper surface of main wing and flap, influenced by propeller slipstream, there are larger low-pressure zone for FBM results than that of power-off results. Comparing (c) and (e), (i) and (k), at the same AOA, with the increase of propulsion thrust, low-pressure zone is enlarged further for both upper surface of main wing and flaps.

As shown in Fig. 10 (d), (f), (j), (l), surface pressure contour of steady ADM are compared with that of FBM in Fig. 10 (c), (e), (i), (k). It can be revealed that the two methods, FBM and ADM, have a good agreement. ADM gives reasonable slipstream influences on wing and flaps.

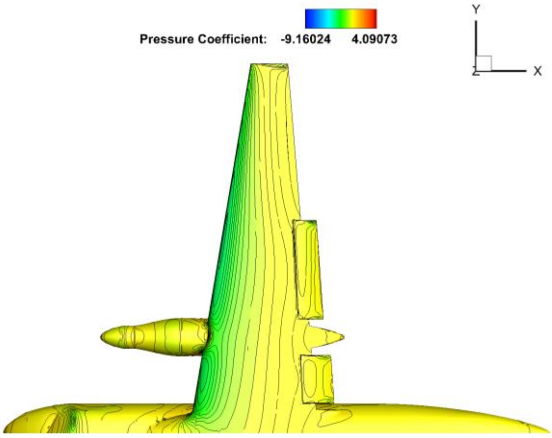

(a) Ma_∞=0.2110, α=8°, power-off

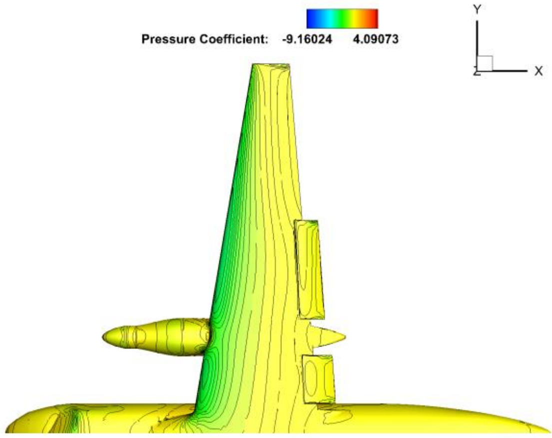

(b) Ma_∞=0.1474, α=8°, power-off

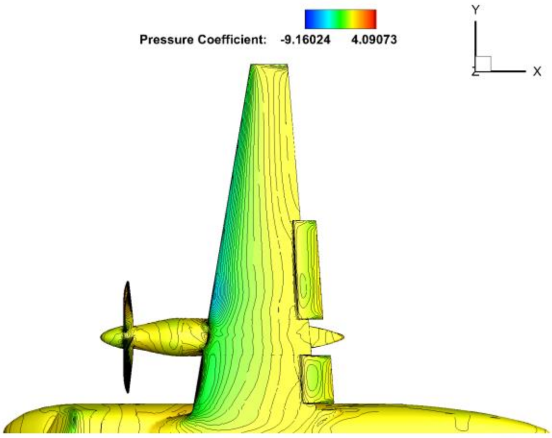

(c) J=1.0, α=8°, FBM

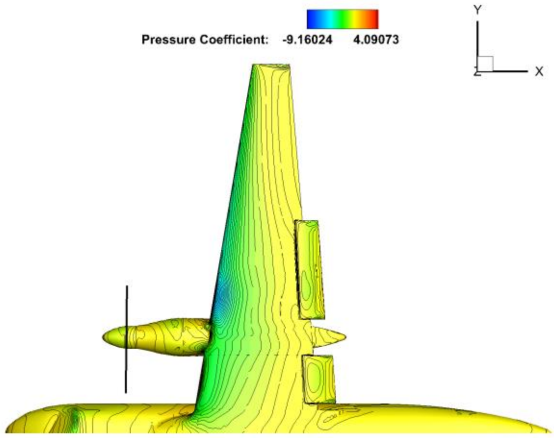

(d) J=1.0, α=8°, ADM

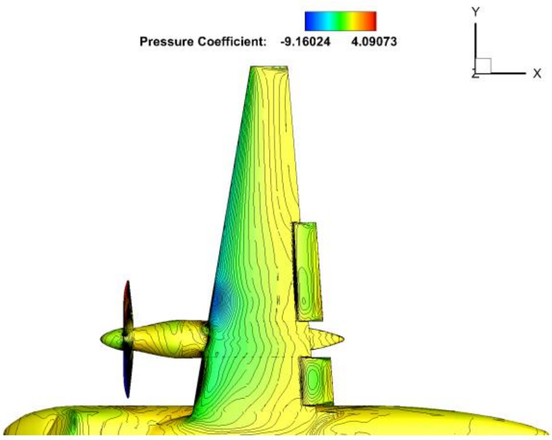

(e) J=0.7, α=8°, FBM

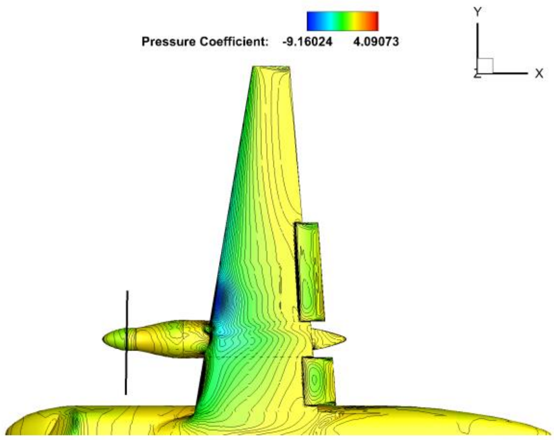

(f) J=0.7, α=8°, ADM

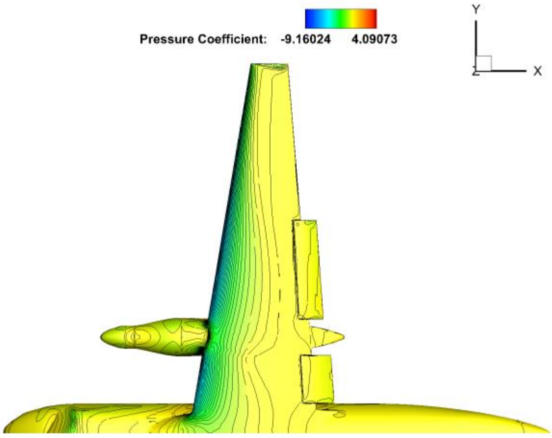

（g） Ma∞=0.2110, α=16°, power-off

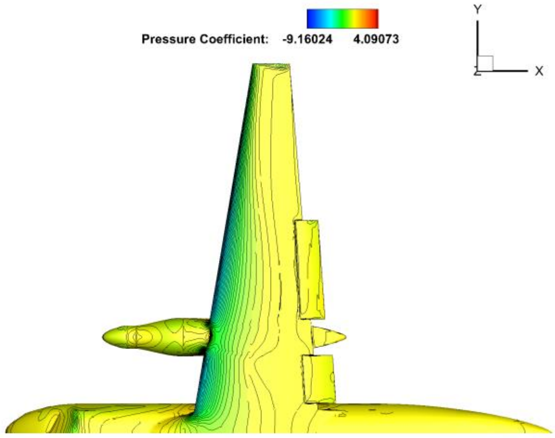

（h） Ma∞=0.1474, α=16°, power-off

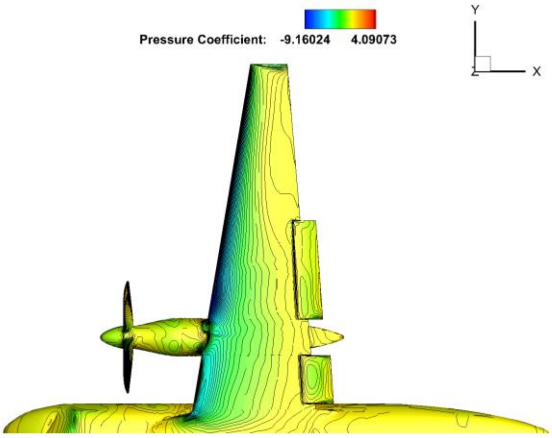

（i） J=1.0, α=16°, FBM

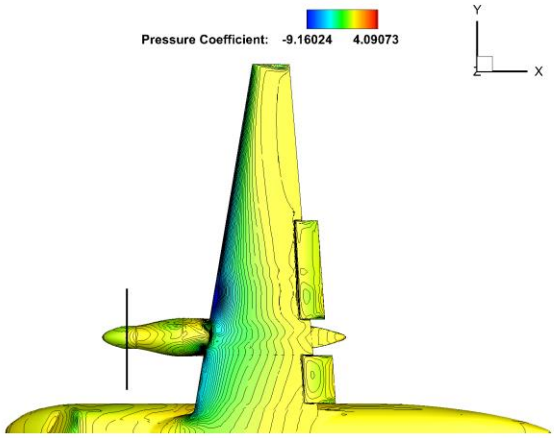

（j） J=1.0, α=16°, ADM

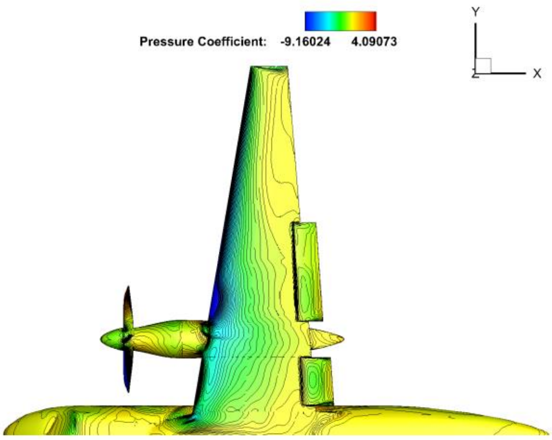

（k） J=0.7, α=16°, FBM

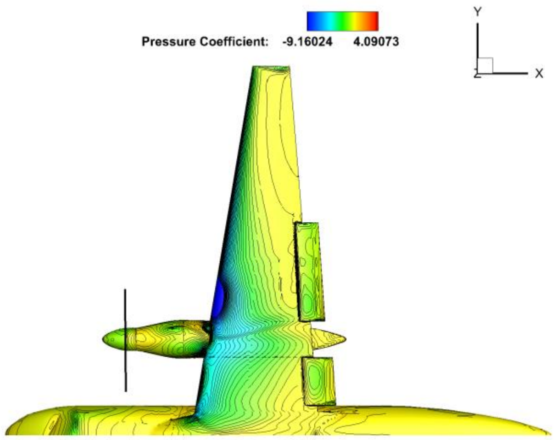

（l） J=0.7, α=16°, ADM

Fig. 10 surface pressure contour distribution

4.5. Detailed analysis of slipstream influences

Five spanwise sections on the wing are provided, including y/b=0.14, y/b=0.36, y/b=0.44, y/b=0.52 and y/b=0.64. Power-off results, FBM results and steady ADM results are presented. All FBM pressure distributions are time averaged. Fig. 11 indicates five positions on the wing where the pressure distributions will be provided. Fig. 12 shows pressure distributions of main wing and flaps at different positions at J=1.0 and J=0.7, with α=8° and α=16°.

Results in Fig. 12 (a) to Fig. 12 (ff) are pressure distribution of wing and flap, while Fig. 12 (gg) to Fig. 12 (ii) only include that of a bare wing. It can be revealed from Fig. 12 that pressure distribution on the wing and flaps are significantly influenced by slipstream, especially in the slipstream zone. Comparing steady ADM results with time averaged FBM results, Fig. 12 indicates that steady ADM results have a good agreement with FBM results. In the region swept by the slipstream with upwash, ADM results have a good agreement with FBM on upper and lower surface. In the downwash swept region, ADM results have a good agreement with full FBM on upper surface, but not on lower surface. Comparing pressure distribution at different advance ratios, it can be noticed that the stronger slipstream leads to larger pressure disturbance on upper and lower surface compared with power-off condition, and difference between the results of ADM and FBM becomes more evident.

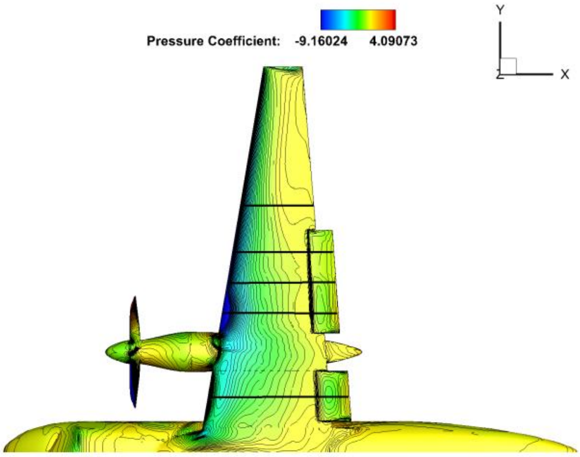

Fig. 11 display of slices location

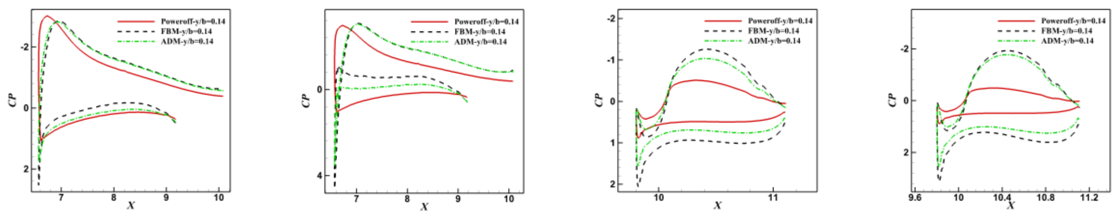

(a) J=1.0, α=8°, wing at y/b=0.14

(b) J=0.7, α=8°, wing at y/b=0.14

(c) J=1.0, α=8°, flap at y/b=0.14

(d) J=0.7, α=8°, flap at y/b=0.14

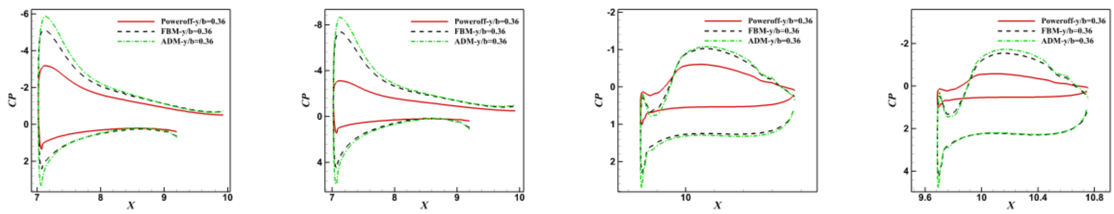

(e) J=1.0, α=8°, wing at y/b=0.36

(f) J=0.7, α=8°, wing at y/b=0.36

(g) J=1.0, α=8°, flap at y/b=0.36

(h) J=0.7, α=8°, flap at y/b=0.36

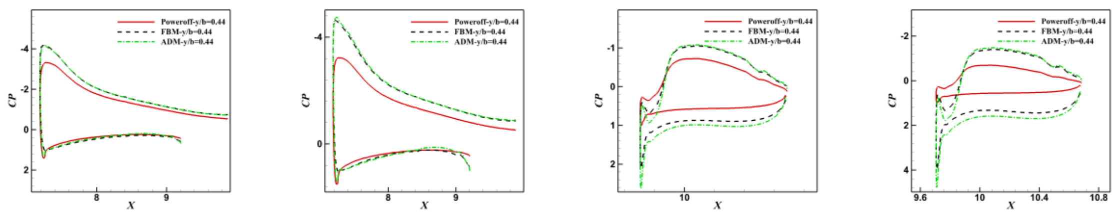

(i) J=1.0, α=8°, wing at y/b=0.44 | (j) J=0.7, α=8°, wing at y/b=0.44 | (k) J=1.0, α=8°, flap at y/b=0.44 | (l) J=0.7, α=8°, flap at y/b=0.44

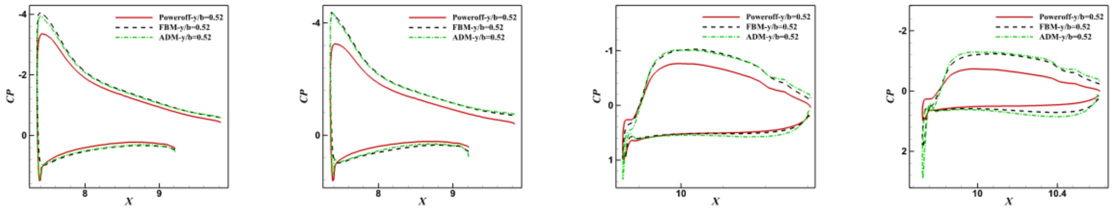

(m) J=1.0, α=8°, wing at y/b=0.52 | (n) J=0.7, α=8°, wing at y/b=0.52 | (o) J=1.0, α=8°, flap at y/b=0.52 | (p) J=0.7, α=8°, flap at y/b=0.52

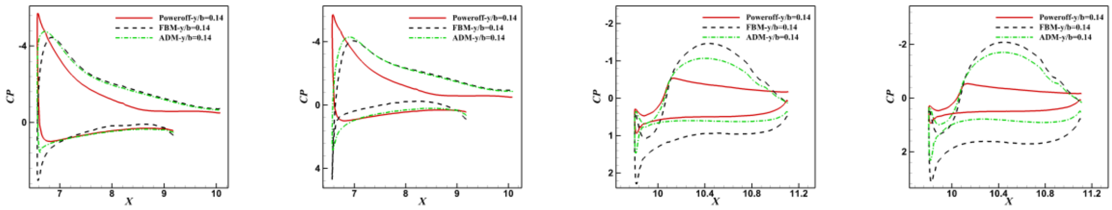

(q) J=1.0, α=16°, wing at y/b=0.14 | (r) J=0.7, α=16°, wing at y/b=0.14 | (s) J=1.0, α=16°, flap at y/b=0.14 | (t) J=0.7, α=16°, flap at y/b=0.14

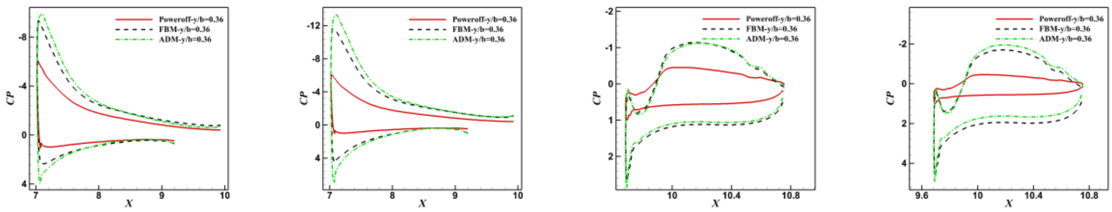

(u) J=1.0, α=16°, wing at y/b=0.36 | (v) J=0.7, α=16°, wing at y/b=0.36 | (w) J=1.0, α=16°, flap at y/b=0.36 | (x) J=0.7, α=16°, flap at y/b=0.36

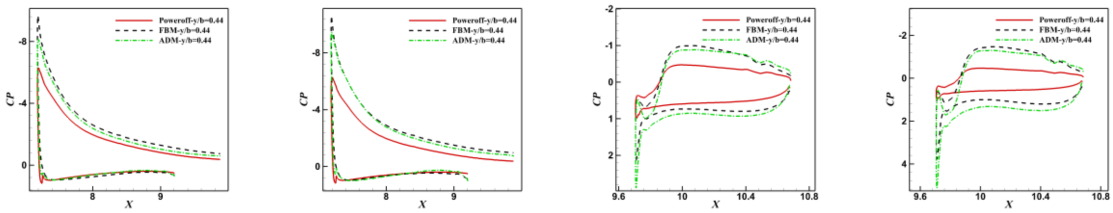

(y) J=1.0, α=16°, wing at y/b=0.44 | (z) J=0.7, α=16°, wing at y/b=0.44 | (aa) J=1.0, α=16°, flap at y/b=0.44 | (bb) J=0.7, α=16°, flap at y/b=0.44

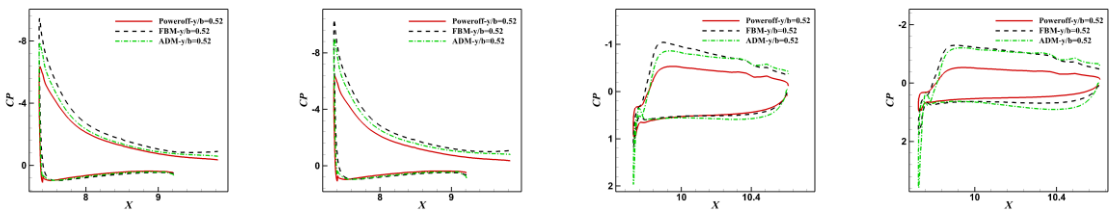

(cc) J=1.0, α=16°, wing at y/b=0.52 | (dd) J=0.7, α=16°, wing at y/b=0.52 | (ee) J=1.0, α=16°, flap at y/b=0.52 | (ff) J=0.7, α=16°, flap at y/b=0.52

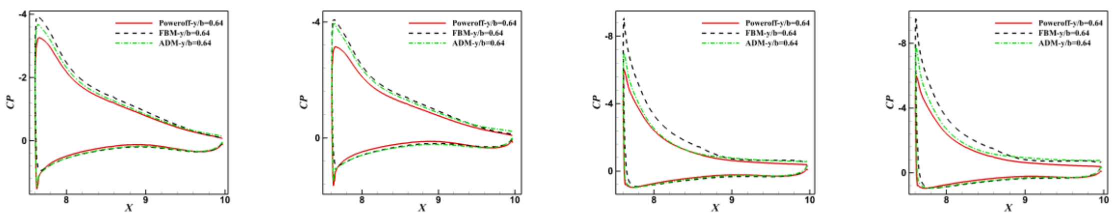

(gg) J=1.0, α=8°, wing at y/b=0.64 | (hh) J=0.7, α=8°, wing at y/b=0.64 | (ii) J=1.0, α=16°, wing at y/b=0.64 | (jj) J=0.7, α=16°, wing at y/b=0.64

Fig. 12 Comparison of surface pressure curves

4.6. Comparison of lift and drag results

In Table 4, the ADM takes around 170 CPU hours compared to around 3100 CPU hours for the unsteady rotating FBM per simulation, making the FBM simulations around 18 times more computationally expensive per simulation.

Table 4 Comparison of mesh sizes and approximate simulation times

	FBM	ADM
No. of points	46,000,000	42,000,000
Approximate CPU hrs taken	3100	170

Table 5 provides the increasement of lift and drag coefficient at different advance ratios.

$$\Delta C_{i(i=L,D)} = C_{i(i=L,D)}^{FBM} - C_{i(i=L,D)}^{power-off} \tag{8}$$

Table 6 provides lift and drag coefficient fractional difference(Δ) between FBM and ADM at two advance ratios.

$$\Delta = \left| C_{i(i=L,D)}^{FBM} - C_{i(i=L,D)}^{ADM} \right| / C_{i(i=L,D)}^{FBM} \tag{9}$$

Fig. 13 (a) compares lift curve of three different cases, power-off, FBM and ADM at different advance ratios.

The above comparison gives evident fact that, for both advance ratios, the lift curve slope with slipstream influence is larger than that of power-off case, and stronger the thrust, larger the lift curve slope. For power-off results and FBM results at both advance ratios, the stall appears at α=16°, ADM predicts a delayed stall. From α=-4~20°, the Δ of lift simulated by ADM and FBM is below 7%.

Fig. 13 (b) provides drag coefficient at different advance ratios and three simulation cases. It can be revealed that slipstream increases total drag of aircraft. The stronger the driven power is, the greater the drag increasement. For both advance ratios, the Δ of drag simulated by ADM and FBM is under 11% from α=-4~16°.

Table 5 lift and drag increasement due to propeller slipstream

		α=-4°	α=0°	α=4°	α=8°	α=12°	α=16°	α=20°	α=24°	α=28°
ΔC_L	J=1.0	0.11	0.14	0.20	0.31	0.47	0.72	0.58	0.65	-
	J=0.7	0.25	0.32	0.41	0.55	0.73	1.01	1.09	1.02	0.95
ΔC_D	J=1.0	0.02	0.03	0.05	0.09	0.14	0.20	0.28	0.33	-
	J=0.7	0.05	0.06	0.10	0.15	0.24	0.36	0.51	0.55	0.67

Table 6 comparison of FBM and ADM results

			α=-4°	α=0°	α=4°	α=8°	α=12°	α=16°	α=20°	α=24°	α=28°
C_L	J=1.0	FBM	0.629	1.068	1.498	1.945	2.358	2.669	2.363	2.284	-
		ADM	0.613	1.072	1.530	1.962	2.304	2.505	2.497	2.280	-
		Δ	2.56%	0.41%	2.14%	0.90%	2.31%	6.14%	5.67%	0.18%	-
	J=0.7	FBM	0.773	1.225	1.676	2.140	2.569	2.943	2.915	2.701	2.571
		ADM	0.763	1.265	1.765	2.271	2.690	2.965	3.114	3.101	3.014
		Δ	1.31%	3.27%	5.31%	6.15%	4.68%	0.73%	6.81%	14.81%	17.24%
C_D	J=1.0	FBM	0.074	0.107	0.163	0.249	0.357	0.478	0.666	0.848	-
		ADM	0.073	0.108	0.167	0.249	0.349	0.451	0.526	0.624	-
		Δ	1.26%	0.49%	2.22%	0.01%	2.19%	5.74%	21.15%	26.39%	-
	J=0.7	FBM	0.101	0.144	0.213	0.320	0.459	0.637	0.889	1.063	1.295
		ADM	0.108	0.155	0.232	0.353	0.502	0.646	0.794	0.896	0.980
		Δ	6.55%	7.59%	8.70%	10.37 %	9.27%	1.41%	10.68%	15.67%	24.29%

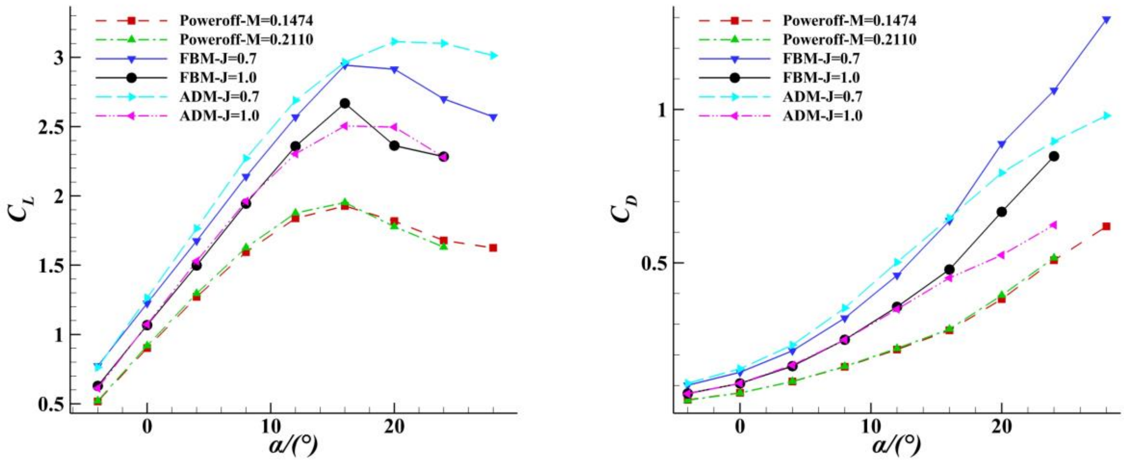

（a） lift coefficient curves （b） drag coefficient curves

Fig. 13 Comparison of lift drag properties

5. Conclusions

The numerical simulations of present research are focused on a propeller aircraft in high lift configuration. Taking the unsteady full rotating propeller CFD results as the reference, ADM is verified in simulate slipstream influence for high lift configuration. As the driven source of slipstream is introduced as a special boundary condition into the steady flow simulation, the CPU time is dramatically reduced than FBM. We have the following conclusions:

1) Although actuator disk loads have a slight difference transitioned from isolated propeller scenarios to full aircraft configurations, the predicted propeller slipstream results are almost identical. This makes the establishment of an actuator disk loads database faster and avoids complex grid generation efforts.
2) By comparing results carried out by steady ADM with unsteady FBM, the lift-drag results, as well as the more detailed pressure distribution, shares a good agreement before the stall. It verifies that ADM can effectively simulate the influences on high lift configuration of propeller slipstream.
3) Based on numerical simulations, it can be concluded that propeller slipstream has significant influences on the high lift configuration. Slipstream boosts lift during takeoff and climb period. In present study, it shows that stronger the thrust, the larger the lift curve slope will be, by fixing the propeller rotating speed with different freestream velocity.
4) Applying ADM, the difficulty of grid generation is reduced. Furthermore, as ADM is conducted with steady simulation, it saves great amount of CPU time compared with unsteady FBM. With the reasonable accuracy, ADM can be used as a fast and primary tool for evaluation of high lift devices.
5) The lift and drag results computed by ADM and FBM begin to diverge near and beyond the stall, more in-depth and detailed research work may be necessary for the unsteady fluctuation influence.

References

[1] Liu P Q. The theorem and application of aero-propeller[M]. Beijing: Beihang University of Aeronautics and Astronautics, 2006: 152. [Chinese].
[2] O'Brien, D. M., Jr. (2006). Analysis of computational modeling techniques for complete rotorcraft configurations (Order No. 3212277). Retrieved from https://www.proquest.com
[3] Tsubasa Ikami, Koji Fujita, and Hiroki Nagai, “Unsteady Flow Field on Wing Surface in Propeller Slipstream at Low Reynolds Number,” AIAA AVIATION 2022 Forum, Jun. 2022.
[4] Chen Xue, Zhou Zhou, Propeller-wing coupled aerodynamic design based on desired propeller slipstream, Aerospace Science and Technology, Volume 97, 2020, 105556, ISSN 1270-9638,
[5] Spalart PR, Venkatakrishnan V. On the role and challenges of CFD in the aerospace industry. *The Aeronautical Journal*. 2016;120(1223):209-232. doi:10.1017/aer.2015.10
[6] Bousquet J M, Gardarein P. Improvements on computations of high-speed propeller unsteady aerodynamics[J]. Aerospace science and technology, 2003, 7(6): 465-472.
[7] Roosenboom E W M, Stürmer A, Schröder A. Advanced experimental and numerical validation and analysis of

propeller slipstream flows [J]. Journal of Aircraft, 2010, 47(1): 284-291.
[8] Xiaoliang Gong, Yong Yang, Zhenfeng Xia. Unsteady Simulation Method and Actuator Disk Theory in Numerical Simulations of Propeller's Interference on Wing [J]. Aeronautical Computing Technique,2012,24(1):76-79. DOI: 10.3969/j.issn.1671-654X.2012.01.021 [Chinese].
[9] Zhenfeng Xia, Song Luo, Yong Yang. Numerical Simulation of propeller slip-stream influence with Actuator Disk Method [J]. ACTA AERODYNAMICA SINICA,2012,30(2):219222, 232. DOI: 10.3969/j.issn. 0258-1825.2012.02.015 [Chinese].
[10] Cusati, V.; Corcione, S.; Nicolosi, F.; Zhang, Q. Improvement of Take-Off Performance for an Electric Commuter Aircraft Due to Distributed Electric Propulsion. Aerospace 2023, 10, 276
[11] Bo Li, Dewang Liang, Guoping Huang. Propeller Slipstream Effects on Aerodynamic Performance of Turbo-prop Airplane Based on Equivalent Actuator Disk Model[J]. Journal of Aeronautics, 2008, 29(4): 845-852 [Chinese].
[12] Le Chuiton F. Actuator disk modelling for helicopter rotors [J]. Aerospace Science and Technology, 2004, 8(4): 285-297.
[13] Khier W. Time-accurate versus Actuator disk simulations of complete helicopters [A]. Nage W E, Resch M and Jäger W. High Performance Computing in Science and Engineering' 05 [C]. Springer, 2006: 209-220.
[14] Veldhuis L L M. Review of Propeller-Wing Aerodynamic Interference [C]//24th International Congress of the Aeronautical Sciences, 29 August - 3 September, 2004, Yokohama, Japan.
[15] Samant S S, Yu N J. Flow prediction for propfan engine installation effects on transport aircraft at transonic speeds [R]. NASA CR-3954, 1986.
[16] Moens F, Gardarein P. Numerical simulation of the propeller/wing interaction for transport aircraft [R]. AIAA Paper: 2001-2404, 2001.
[17] Zachariadis A, Hall C A. Application of a Navier-Stokes solver to the study of open rotor aerodynamics [J]. Journal of Turbomachinery, 2011, 133(3): 031025.
[18] Raichle A, Melber-Wilkending S, Himisch J. A new actuator disk model for the TAU code and application to a sailplane with a folding engine [C] // Notes on Numerical Fluid Mechanics and Multidisciplinary Design: New Results in Numerical and Experimental Fluid Mechanics VI, Contributions to the 15th STAB/DGLR Symposium Darmstadt, Germany, 2006, Vol. 96, 2007: 52-61.
[19] Strash D J, Lednicer D A, Rubin T D. Analysis of propeller-induced aerodynamic effects [R]. AIAA Paper: 1998-2414, 1998.
[20] Amato M, Boyle F, Eaton J A, et al. Euler/Navier stokes simulation for propulsion-airframe integration of advanced propeller driven aircraft in the European research programs GEMINI/APIAN [C] // 21st ICAS Congress, 13-18 September, 1998, Melbourne, Australia.
[21] Christopher Wales, Dorian Jones, Ann Gaitonde, Peter Risley-Settle, and Andrew Peace, "Comparison of Aircraft Loads Using URANS and Actuator Disk Modelling of Propellers," AIAA AVIATION 2022 Forum. American Institute of Aeronautics and Astronautics, 15-Jun-2022.
[22] Christopher Wales, Dorian Jones, Ann Gaitonde, Peter Risley-Settle, and Andrew Peace, "Comparison of Aircraft Loads Using URANS and Actuator Disk Modelling of Propellers at High Incidence." American Institute of Aeronautics and Astronautics.
[23] A. D. Ronch, D. Vallespin, M. Ghoreyshi, and K. J. Badcock, "Evaluation of Dynamic Derivatives Using Computational Fluid Dynamics," vol. 50, no. 2. American Institute of Aeronautics and Astronautics, pp. 470–484.
[24] Anderson, J. D., Computational Fluid Dynamics: The Basic with Applications, Mechanical Engineering Series, McGraw–Hill, New York, 1995, pp. 49–74.
[25] Wei Wang, Yong Yang, Zhenfeng Xia. Study on Comparison of Different Numerical Simulation Methods Concerning Propeller Slipstream [J]. Aeronautical Computing Technique,2012,42(5):80-83,86. DOI: 10.3969/j.issn.1671-654X.2012.05.020 [Chinese].